IJMMM International Journal of Minerals, Metallurgy and Materials 矿物冶金与材料学报（英文版）

Effect of Nb–V microalloying on the hot deformation behavior of medium Mn steels

Yumeng Wang, Qinyi Guo, Bin Hu, and Haiwen Luo

Cite this article as:
Yumeng Wang, Qinyi Guo, Bin Hu, and Haiwen Luo, Effect of Nb–V microalloying on the hot deformation behavior of medium Mn steels, *Int. J. Miner. Metall. Mater.*, 32(2025), No. 2, pp. 360-368. https://doi.org/10.1007/s12613-024-2914-8

INTERNATIONAL JOURNAL OF
Minerals, Metallurgy and Materials

Volume 32, Number 2, February 2025
Page 360

Research Article https://doi.org/10.1007/s12613-024-2914-8

Effect of Nb–V microalloying on the hot deformation behavior of medium Mn steels

Yumeng Wang, *Qinyi Guo*, *Bin Hu*, *and Haiwen Luo*✉

School of Metallurgical and Ecological Engineering, University of Science and Technology Beijing, Beijing 100083, China
(Received: 8 March 2024; revised: 10 April 2024; accepted: 15 April 2024)

Abstract: The influence of Nb–V microalloying on the hot deformation behavior and microstructures of medium Mn steel (MMS) was investigated by uniaxial hot compression tests. By establishing the constitutive equations for simulating the measured flow curves, we successfully constructed deformation activation energy (Q) maps and processing maps for identifying the region of flow instability. We concluded the following consequences of Nb–V alloying for MMS. (i) The critical strain increases and the increment diminishes with the increasing deformation temperature, suggesting that NbC precipitates more efficiently retard dynamic recrystallization (DRX) in MMS compared with solute Nb. (ii) The deformation activation energy of MMS is significantly increased and even higher than that of some reported high Mn steels, suggesting that its ability to retard DRX is greater than that of the high Mn content. (iii) The hot workability of MMS is improved by narrowing the hot processing window for the unstable flow stress, in which fine recrystallized and coarse unrecrystallized grains are present.

Keywords: medium manganese steel; niobium–vanadium microalloying; flow behavior; dynamic recrystallization; hot workability

1. Introduction

For crash safety, a lightweight design is an effective way for the automotive industry to improve fuel efficiency and reduce CO_2 emissions. Advanced high-strength steels (AHSSs) emerge as a viable solution, catering to the industry's trifecta of priorities, namely, economic viability, environmental sustainability, and safety enhancement. AHSSs have been developed into the third generation (3rd Gen) and have garnered considerable attention owing to their exceptional mechanical properties and heightened cost competitiveness [1–4]. Medium Mn steels (MMSs) with Mn concentrations in the range of 4wt%–10wt% have been widely regarded as promising candidates for 3rd Gen AHSSs. To date, the industrialized production of 3rd Gen AHSSs is still highly restricted by many processing difficulties [5–6]. In hot working, the metal experiences work hardening during plastic straining and softening due to dynamic recovery (DRV) and dynamic recrystallization (DRX). Cross-slip and climb of dislocations are usually difficult to achieve in the austenite of MMSs during hot deformation due to low stack fault energy. Hence, DRX is preferred over DRV. DRX can eliminate dislocations and even the cracks generated by work hardening and refine the prior austenite grains [7–10]. The optimization of hot deformation parameters through flow behavior modeling is of paramount significance in delineating the industrial processing parameters of MMSs. Sun *et al.* [11] established a finite element model for the hot compression of 0.15C–7Mn steel to derive the DRXed fraction and the average grain sizes under different hot deformation conditions using DEFORM software, and the findings are in good agreement with the experimental results. Liu *et al.* [12] established a critical strain model on the DRX of 0.22C–8.5Mn steel using the *P*–*J* double differential method and finally constructed the hot processing maps for determining the optimal processing window.

Nb and V are often added into MMSs as microalloying elements for grain refinement and precipitation strengthening [13–14]. Current studies mainly focus on the effects of Nb and V microalloying on mechanical properties and microstructure evolution. Luo *et al.* [15] found that 0.04wt%Nb microalloying significantly improved the hydrogen embrittlement resistance of hot-rolled 7Mn–3.5Ni–1.5Cu–0.08C steel. Nb addition resulted in a high C concentration at the prior austenite grain boundaries (PAGBs) and the formation of filmy retained austenite along the PAGBs, which served as a suitable hydrogen-trapping site that reduced hydrogen diffusion and thus inhibited the occurrence of hydrogen-induced cracks. By contrast, Varanasi *et al.* [16] reported that Nb addition was detrimental to the nucleation and growth of austenite during the intercritical annealing of cold-rolled 10Mn–0.05C–1.5Al steel, leading to reduced retained austenite fraction and deteriorated plasticity. Zhu *et al.* [17] showed that Nb and V addition to hot-rolled 0.3C–9Mn–

✉ Corresponding author: Haiwen Luo E-mail: luohaiwen@ustb.edu.cn

2.5Al steel significantly increased the yield strength and had almost no detrimental effect on ductility.

The effects of Nb–V addition on the hot deformation behavior of MMSs remain largely unexplored. In this study, the hot deformation behaviors of MMSs with and without Nb–V were investigated systematically by hot compression tests. The constitutive equations were established for the two steels to describe the flow behavior during hot deformation, and the resultant processing maps and microstructures for the two steels were compared.

2. Methods

The nominal chemical compositions of the two studied steels are listed in Table 1. Both contained approximately 0.1wt% C, 5wt% Mn, and 2wt% Al; one was microalloyed with Nb and V (termed 5MnNbV), and the other was not (5Mn).

Table 1. Chemical composition of the studied MMSs wt%

MMS	C	Mn	P	S	N	Al	V	Nb
5Mn	0.11	4.89	0.005	0.002	0.002	1.96	—	—
5MnNbV	0.11	4.90	0.005	0.003	0.002	1.96	0.19	0.0079

Thermodynamic calculations on the two steels were performed using Thermo-Calc software with the database of TCFE9. The calculation results in Fig. 1 indicated that Ae_3 temperatures, the ortho-equilibrium austenite-to-ferrite transformation temperatures, of 5Mn and 5MnNbV steels are 929°C and 972°C, respectively, and NbC and VC have completely dissolved at 1180°C and 848°C, respectively. In the temperature range of 1000–1150°C employed for hot compression, both steels are in the austenitic region, and V cannot precipitate as carbide in austenite. By contrast, NbC can precipitate and gradually dissolve with the increasing temperature.

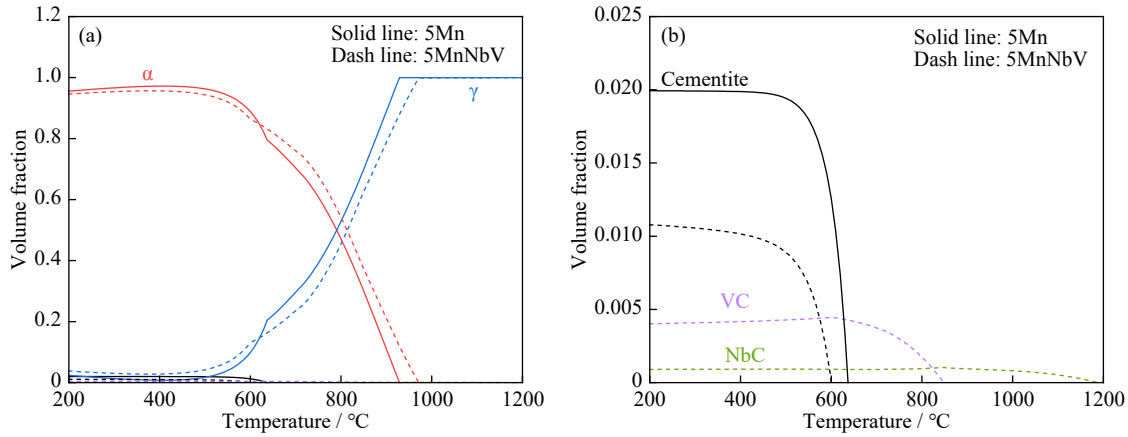

Fig. 1. (a) Temperature dependence of equilibrium volume fraction of different phases for the two steels calculated by Thermo-Calc software and (b) enlarged view on precipitations.

The alloys were melted in a 50-kg vacuum-induced furnace and then hot forged into rectangular billets. The cylindrical specimens with a diameter of 8 mm and a height of 12 mm were machined for the hot compression experiments. Unidirectional compression tests were performed on a Gleeble 3800 thermo-mechanical simulator. Tantalum sheets with a thickness of 0.1 mm were glued with conductive adhesive between the specimen and the anvil to provide isolation and lubrication. Hot compression experiments were conducted at temperatures ranging from 1000 to 1150°C with an interval of 50°C and a strain rate range of 0.001–1 s^{-1}. The specimens were first heated to 1200°C with 10°C/s for 300 s, followed by cooling to the target temperature with 10°C/s for 60 s before compression. All the specimens were compressed to a true strain of 0.6 at the specified strain rate, followed by immediate water quenching to room temperature to preserve their microstructures.

Microstructures were examined under optical microscope and transmission electronic microscope (TEM) attached with energy dispersive spectrum (EDS) in the central section of the compressed specimen cut by a wire parallel to the compression direction after standard grinding, polishing, and etching in the saturated picric acid at 63°C. The statistic results on the prior austenite grain sizes (PAGSs) in the specimens were derived with ImageJ software.

3. Results and discussion

3.1. Flow behavior during hot compression

Fig. 2 shows the flow stress curves of the two studied steels at different temperatures and strain rates ($\dot{\varepsilon}$). In all the curves, work hardening exists at the initial stage of deformation, implying significant dislocation multiplication. With further straining, the deformation storage energy increases gradually until it reaches a critical value to trigger DRX. Subsequently, the flow stress starts to decrease with strain due to the dynamic softening effect. Changes in the flow stress essentially reflect the competition between the propagation and

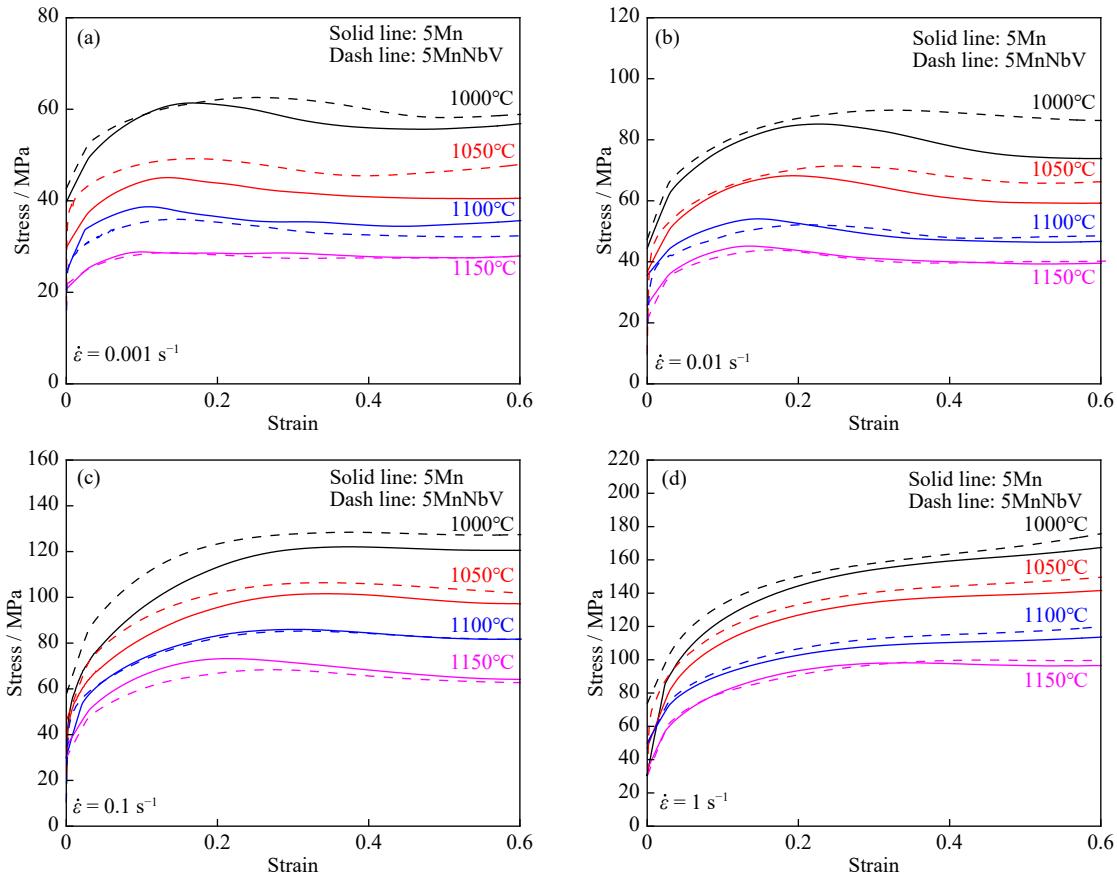

Fig. 2. Flow stress–strain curves of the experimental MMSs at different deformation conditions: (a) $\dot{\varepsilon}$ = 0.001 s^{-1}; (b) $\dot{\varepsilon}$ = 0.01 s^{-1}; (c) $\dot{\varepsilon}$ = 0.1 s^{-1}; (d) $\dot{\varepsilon}$ = 1 s^{-1}.

annihilation of dislocations [18]. When the work hardening and softening mechanisms reach a dynamic equilibrium, the flow curves flatten out. Pronounced peak stresses are widely indicative of DRX. For the flow stress curve without a distinct peak, DRV is generally the main softening mechanism under the corresponding deformation conditions. Some studies claim that DRX may occur even in the absence of a significant peak in the flow curves [19–20]. Especially at high strain rates, dislocations proliferate rapidly, and the work hardening effect is enhanced to such an extent that the softening mechanism is difficult to overcome.

When the strain rate is constant, the flow stress decreases with the increasing temperature because many dislocations are annihilated, and grains grow rapidly at high temperatures [11,21]. When the temperature is constant, the flow stress increases with the strain rate because dislocations build up rapidly, and stress concentrations cannot be released. A low strain rate can provide additional time for the rearrangement and annihilation of dislocations [22].

Fig. 3 illustrates the TEM and EDS results on the precipitates in 5MnNbV steel after solution treatment at 1200°C and hot compression at 1000°C with a strain rate of 0.001 s^{-1}. The

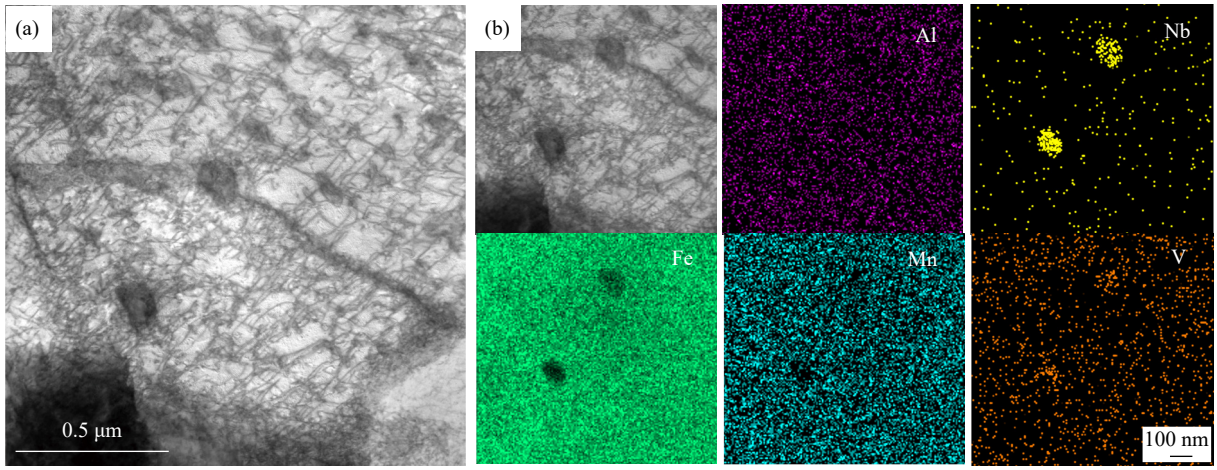

Fig. 3. TEM and EDS results of 5MnNbV after hot deformation at 1000°C with a strain rate of 0.001 s^{-1}: (a) TEM bright-field image of 5MnNbV; (b) EDX maps of the precipitates.

nanosized particles precipitate at grain boundaries and dislocations and have a size of (107.5 ± 14.2) nm, as shown in Fig. 3(a). Energy dispersive X-ray spectroscopy (EDX) compositional examination in Fig. 3(b) indicates that the particles are mainly enriched with Nb, i.e., NbC.

Fig. 4(a) shows the variation of the peak stress σ_p with deformation temperature and strain rate for both of the studied steels. When hot deformation is performed at the same temperature and strain rate, 5MnNbV exhibits higher σ_p than 5Mn. However, the difference between them decreases with the increase in deformation temperature until 1150°C because many NbC particles are dissolved and get coarse at high temperatures, leading to reduced inhibition on dislocation motion and grain boundary migration.

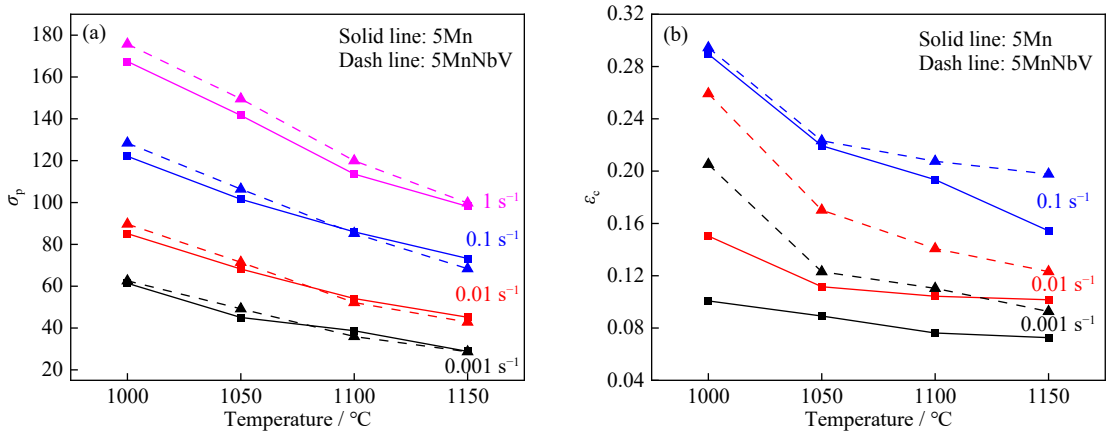

Fig. 4. Temperature dependence of the peak stress σ_p (a) and critical strain ε_c (b) of the two studied MMSs at different strain rates.

Critical strain (ε_c) is the minimum strain required for DRX. Fig. 4(b) shows the critical strains for the two steels as calculated by the *P–J* double differential method [23] at the strain rates of 0.001–0.1 s^{-1}. At 1 s^{-1}, DRX occurs in both steels only at 1150°C, and the critical strains for 5MnNbV are higher than those for 5Mn, suggesting a pronouncedly delayed DRX due to Nb and V addition. In particular, the difference in ε_c for the two studied steels is large and gradually diminishes with the increase in temperature at the low strain rates of 0.001–0.01 s^{-1}, indicating the diminishing inhibition on DRX. Solute Nb and NbC particles can impede DRX. When the strain rate is low, Nb as a solid solution exerts less hindrance to DRX compared with its role as a precipitate within the temperature range considered in this study. This finding is consistent with previous research, stating that the hindering effect of NbC particles on grain boundary migration is usually pronounced in austenite [17].

At 0.1 s^{-1}, the difference in ε_c of the two steels increases with the increase of deformation temperature, which is different from the case at 0.01 and 0.001 s^{-1}. This phenomenon is due to the great difference in deformation time, which is 6, 60, and 600 s for the strain rate of 0.1, 0.01, and 0.001 s^{-1}, respectively. At 0.1 s^{-1}, the time for NbC to dynamically precipitate is insufficient. At low temperatures and high strain rates, the precipitation kinetics of NbC are considerably less favorable. Hence, the two studied steels exhibit comparable critical stresses of DRX during deformation at 1000–1050°C with a strain rate of 0.1 s^{-1}.

DRX leads to the softening of the hot deformed matrix, so the flow stress after DRX is lower than the peak stress. Therefore, the stress (σ) reduction after the peak stress reflects the softening effect as shown in Fig. 5. The 5Mn steel exhibits more pronounced softening at 1000–1150°C after the small peak strain than 5MnNbV, suggesting that Nb–V microalloying delays the onset of DRX and significantly increases the hot strength of the recrystallized matrix. The latter may result from the fine size of recrystallized grains at high temperatures or the low recrystallized extent at low temperatures resulting from Nb–V alloying, which will be discussed later.

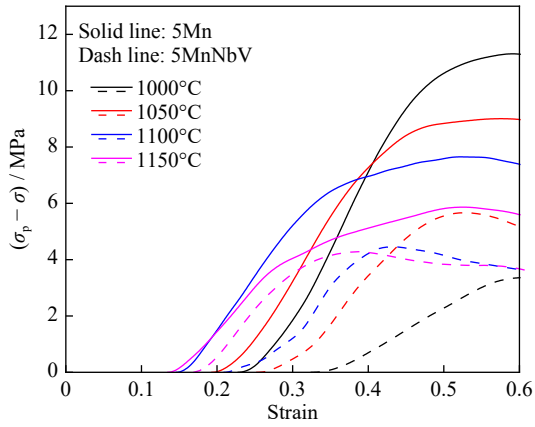

Fig. 5. Influence of Nb–V microalloying on the stress reduction, $\sigma_p - \sigma$, after the peak stress at the strain rate of 0.01 s^{-1}.

3.2. Constitutive equations

During hot working, the hot deformation behavior is influenced by strain, strain rate, deformation temperature, and microalloying elements [18] and is commonly expressed using the Arrhenius equation [24–25]:

$$\dot{\varepsilon} = Af(\sigma)\exp\left(-\frac{Q}{RT}\right) \quad (1)$$

where T, $\dot{\varepsilon}$, and σ are the temperature in K, strain rate in s^{-1}, and stress in MPa, respectively; R is the universal gas constant 8.314 in $J \cdot mol^{-1} \cdot K^{-1}$; Q represents the activation energy for hot deformation in kJ/mol.

The $f(\sigma)$ in Eq. (1) can be described by the power function, the exponential function, and Sellars' hyperbolic sine function as given below [26–27]:

$$\ln\dot{\varepsilon} = n_1 \cdot \ln\sigma + \ln A_1 - \frac{Q}{RT} \tag{2}$$

$$\ln\dot{\varepsilon} = \beta \cdot \sigma + \ln A_2 - \frac{Q}{RT} \tag{3}$$

$$\ln\dot{\varepsilon} = n \cdot \ln[\sinh(\alpha\sigma)] + \ln A - \frac{Q}{RT} \tag{4}$$

where A_1, A_2, A, n_1, n, β, and α are material constants, and σ is usually taken as the peak stress σ_p.

For the constant T, n_1 and β can be derived by linear fitting of $\ln\sigma$ vs. $\ln\dot{\varepsilon}$ plots and σ vs. $\ln\dot{\varepsilon}$ plots, respectively. The stress multiplier α ($\alpha \approx \beta/n_1$) is an adjustable constant that ensures that $\alpha\sigma$ is in the appropriate range, making the $\ln\dot{\varepsilon}$ vs. $\ln[\sinh(\alpha\sigma)]$ plots linear and parallel at constant temperature [28–29]. n is derived by the linear fitting of $\ln[\sinh(\alpha\sigma)]$ vs. $\ln\dot{\varepsilon}$ plots (Fig. 6(a) and (b)). Besides, according to Eq. (4), when the strain rate is constant, the mean value of Q can be derived by the linear fitting of $\ln[\sinh(\alpha\sigma)]$ vs. $1/T$ plots (Fig. 6(c) and (d)). The determined apparent activation energies are 377.775 and 415.722 kJ/mol for 5Mn and 5MnNbV, respectively. Both values are higher than the self-diffusion activation energy of Fe in γ-Fe (280 kJ/mol) [30] and the hot deformation activation energy for plain carbon steels (300 kJ/mol). The Q value of 5Mn steel is lower than those for some high Mn steels, e.g., 391 kJ/mol for Fe–23Mn–2Al–0.2C [31] and 387 kJ/mol for Fe–20Mn–3Si–3Al [32], suggesting that the high contents of Mn, Al, and C in a solution could raise the activation energy because these elements can restrict the movement of dislocations. Meanwhile, Nb and V exhibit stronger retardation than Mn, so the 5MnNbV steel has even higher deformation activation energy than high Mn steels.

The Zener–Hollomon parametric equation is widely used to analyze the effect of deformation temperature and strain rate on the hot deformation behavior of metallic materials [24,33]:

$$Z = \dot{\varepsilon}\exp\left(\frac{Q}{RT}\right) \tag{5}$$

Combination of Eqs. (4) and (5) leads to:

$$\ln Z = \ln A + n\ln[\sinh(\alpha\sigma)] \tag{6}$$

The linear relationship of $\ln Z$ vs. $\ln[\sinh(\alpha\sigma)]$ for the two steels is confirmed, as shown in Fig. 7. A can be determined from the intercept of the linear fittings.

Finally, the constitutive equations are derived by substituting the above-derived parameters into Eq. (1) for the two steels:

$$\dot{\varepsilon}_{5\text{Mn}} = 5.674\times10^{12}[\sinh(0.0133\sigma)]^{4.652}\exp\left(-\frac{377775}{RT}\right) \tag{7}$$

$$\dot{\varepsilon}_{5\text{MnNbV}} = 1.1421\times10^{14}[\sinh(0.0128\sigma)]^{4.366}\exp\left(-\frac{415722}{RT}\right) \tag{8}$$

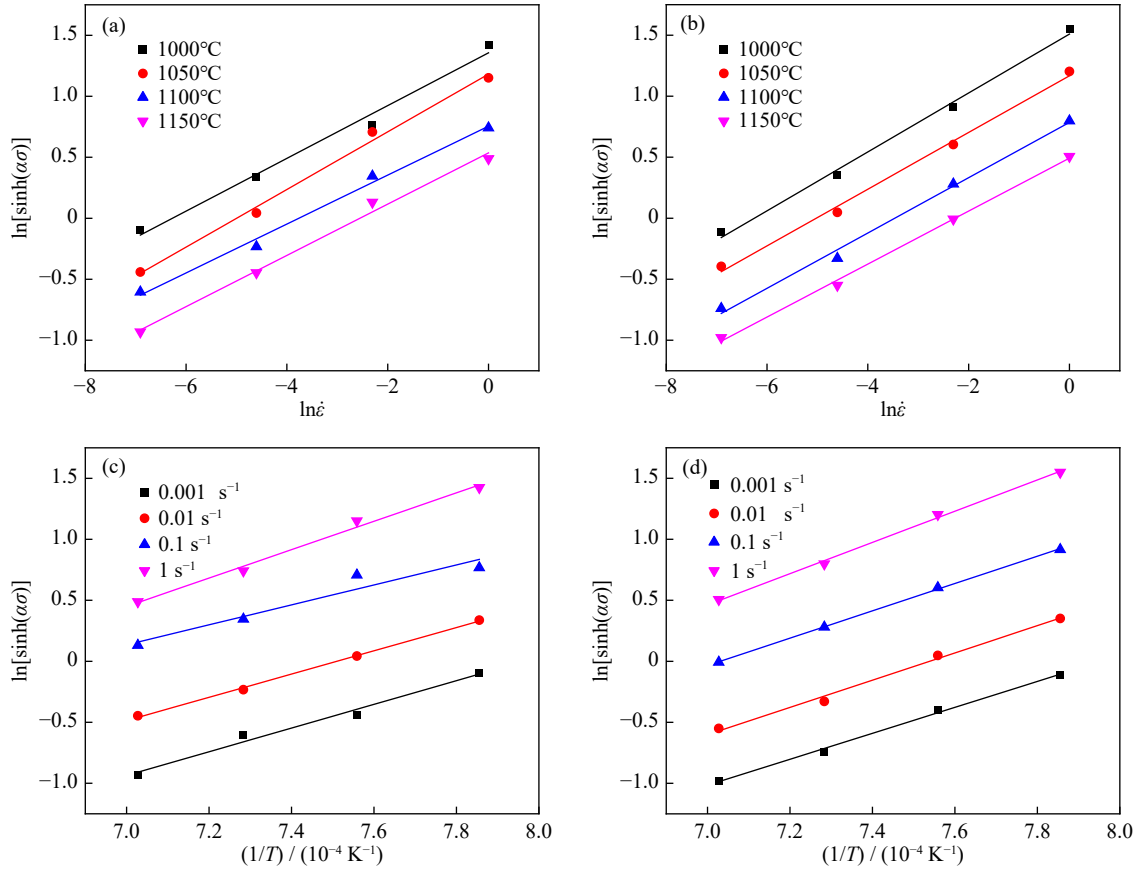

Fig. 6. Relationships curves of $\ln\dot{\varepsilon}$ vs. $\ln[\sinh(\alpha\sigma)]$ and $1/T$ vs. $\ln[\sinh(\alpha\sigma)]$ at the strain of 0.6 for (a, c) 5Mn steel and (b, d) 5MnNbV steel.

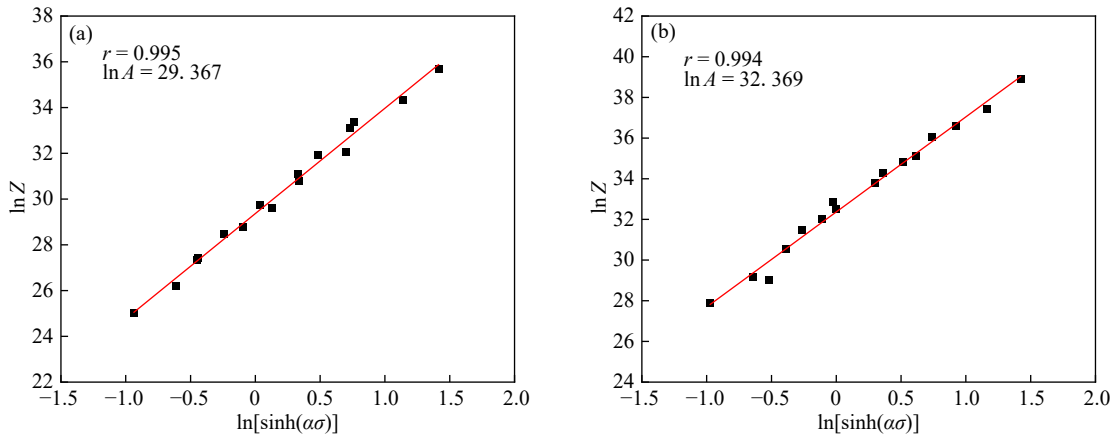

Fig. 7. Relationships between ln Z and ln[sinh($\alpha\sigma$)]: (a) 5Mn and (b) 5MnNbV. r is Pearson's correlation coefficient.

3.3. Activation energy maps

In the foregoing analysis, the average deformation activation energy has been determined for both studied steels. However, the activation energy is actually the resistance to deformation, which depends on the capacity of dislocations to surmount obstacles during plastic deformation and should be strongly influenced by hot deformation parameters, including temperature and strain rate [34]. In this case, a map of activation energy is required to describe the variation of Q with deformation temperature and strain rate. Q can be expressed as:

$$Q = R \cdot \left\{ \frac{\partial(\ln \dot{\varepsilon})}{\partial \ln[\sinh(\alpha\sigma)]} \right\}_T \left\{ \frac{\partial \ln[\sinh(\alpha\sigma)]}{\partial\left(\frac{1}{T}\right)} \right\}_{\dot{\varepsilon}} = R \cdot n(T) \cdot S(\dot{\varepsilon}) \tag{9}$$

The values of n and S are obtained from the slopes of the $\ln\dot{\varepsilon}$ vs. ln[sinh($\alpha\sigma$)] plots at different temperatures and the slopes of the ln[sinh($\alpha\sigma$)] vs. $1/T$ plots at different strain rates, respectively. The Q at each temperature and strain rate can be derived by fitting a polynomial to the n–T and S–$\dot{\varepsilon}$ plots and substituting the results into Eq. (9). Fig. 8 shows the variation of calculated Q values with temperature and strain rate for both steels at the strain of 0.6. At 1 s^{-1}, both steels exhibit high activation energy. This phenomenon arises from the reduced time available for dynamic softening and enhanced dislocation multiplication due to work hardening, both increasing the energy requirement for dislocation motion [35].

Q serves as an indicator of the deformation mechanism. A relatively stable and low Q region generally corresponds to the feasible processing window [36], and a region with rapidly changing Q represents the unfavored window. Under the experimental conditions, the Q values of 5Mn and 5MnNbV are in the ranges of 261–498 kJ/mol and 336–499 kJ/mol, respectively. The former shows a large variation in the region of high temperature and high strain rate, which may result in flow instability [37]. Meanwhile, the Q values for 5MnNbV remain notably stable, suggesting its superior hot workability. In the region of low temperature and low strain rate, the Q of 5MnNbV is significantly higher than that of 5Mn because many NbC particles can dynamically precipitate during deformation in this region. In conclusion, Nb–V microalloying results in the overall increase in Q and the reduced the sensitivity of Q to temperature and deformation rate, the latter improving the hot working performance. In addition to the ac-

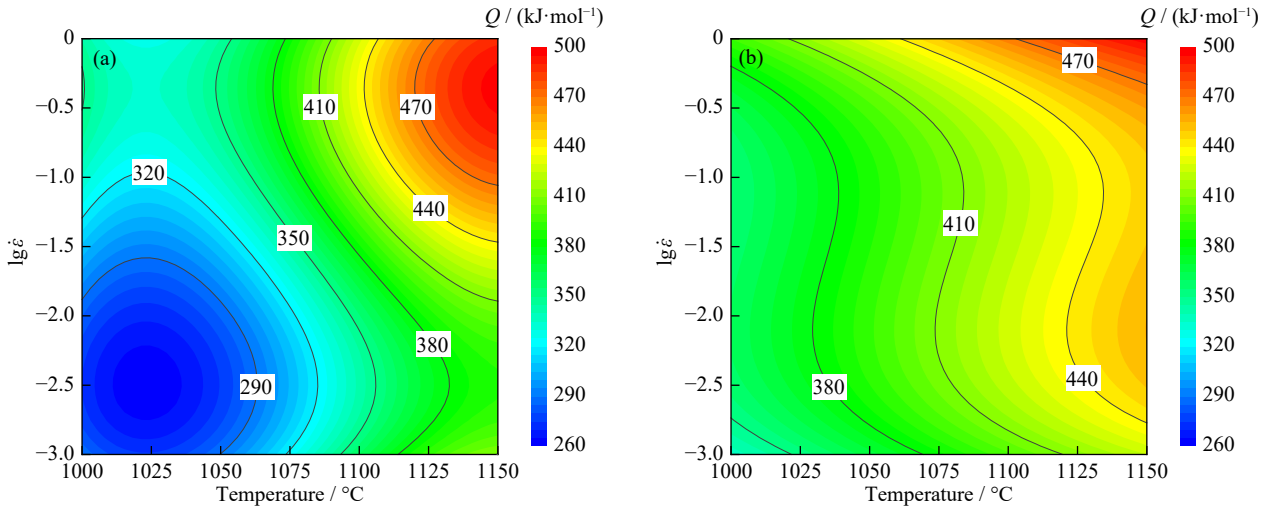

Fig. 8. Hot deformation activation energy (Q) maps for two studied MMSs at the strain of 0.6: (a) 5Mn and (b) 5MnNbV.

tivation energy map, the processing maps based on microstructural analysis are required to determine the optimal processing window.

3.4. Processing maps

Processing maps are an effective way to evaluate the processing performance of materials and are often used to predict and analyze the characteristics and mechanisms of material deformation under different deformation conditions. They are used to optimize the manufacturing process and avoid hot processing defects.

The parameter η is introduced to represent the energy dissipation efficiency due to microstructure evolution and can be expressed as [27]:

$$\eta = \frac{J}{J_{\max}} = \frac{2m}{m+1} \tag{10}$$

where J represents the energy used for microstructure evolution. Its value reaches the maximum ($J_{\max}$) when the material is in an ideal linear dissipative state ($m = 1$). m represents the strain rate sensitivity parameter, which is defined as the ratio of the energy used for microstructural evolution (J) to the energy dissipated by plastic deformation (G):

$$m = \frac{\partial J}{\partial G} = \frac{\dot{\varepsilon}\partial\sigma}{\sigma\partial\dot{\varepsilon}} = \frac{\partial(\ln\sigma)}{\partial(\ln\dot{\varepsilon})} \tag{11}$$

In addition to the favored deformation mechanisms such as DRX for eliminating the original defects in a material, the presence of detrimental mechanisms such as dynamic strain failure, void formation, and adiabatic shear bands can contribute to an increase in the power dissipation rate η. Some supplementary criteria are necessary to assess the processing instability of the material, enabling a discerning judgment and the avoidance of defects during hot processing.

The instability criterion proposed by Prasad and Seshacharyulu [38] suggests that material processing enters the flow instability region when Eq. (12) is satisfied:

$$\xi(\dot{\varepsilon}) = \frac{\partial \ln\left(\frac{m}{m+1}\right)}{\partial \ln \dot{\varepsilon}} + m < 0 \tag{12}$$

where ξ is the instability parameter. When $\xi < 0$, flow instability, such as the appearance of localized flow regions, shear zones, and microcracks, may occur [39]. The power dissipation efficiency and instability parameter are calculated from Eqs. (10) and (12), both are functions of temperature and strain rate. Their results at the same strain are superimposed to obtain the hot processing maps of the two studied steels as shown in Fig. 9. The gray area is the flow instability region, and the numbers on the contours represent the energy dissipation efficiencies. In general, high dissipation efficiencies indicate that the material is suitable for processing under these conditions. The flow instability regions of both studied steels are mainly concentrated in the high-strain-rate region, and the instability region for 5MnNbV is significantly smaller than that for 5Mn. These findings suggest that the Nb–V alloyed steel has a wide processing window for hot working without generating defects.

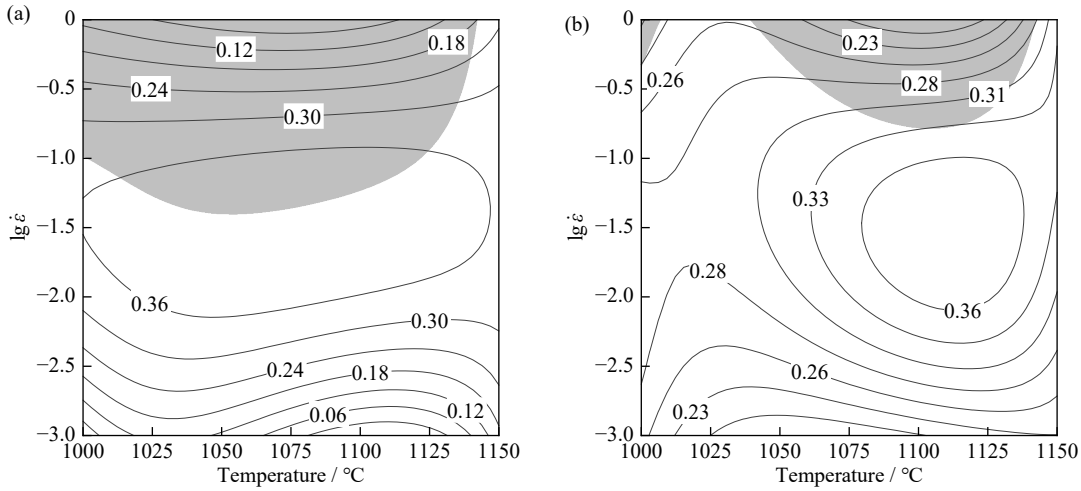

Fig. 9. Processing maps of experimental MMSs at a strain of 0.6: (a) 5Mn and (b) 5MnNbV. The gray area is the region of flow instability, and the numbers on the contours represent the energy dissipation efficiencies.

3.5. Microstructural analysis

The microstructures formed after hot compression at 1100°C with a strain rate of 0.1 s^{-1} are given in Fig. 10(a) and (b). The average grain sizes of 5Mn and 5MnNbV are 20.04 and 15.28 μm, respectively. Fully recrystallized grains are observed in both of them. Some grains in 5Mn have become coarse (Fig. 10(a) and (c)), suggesting that the unfavored mixture of coarse and fine sizes is formed under this processing condition. In 5MnNbV, uniformly distributed fine PAGS is found due to the presence of either solute Nb or fine NbC. This result is consistent with those observed under deformation in the unstable region in Fig. 9(a) and the stable region in Fig. 9(b). The microstructures formed after hot compression at 1100°C with 1 s^{-1}, i.e., the unstable region in Fig. 9 for the two studied steels, are given in Fig. 10(c) and (d). The microstructures in both specimens are a mixture of fine DRXed and coarse deformed grains, indicating an unstable state during hot working. Therefore, the microstructur-

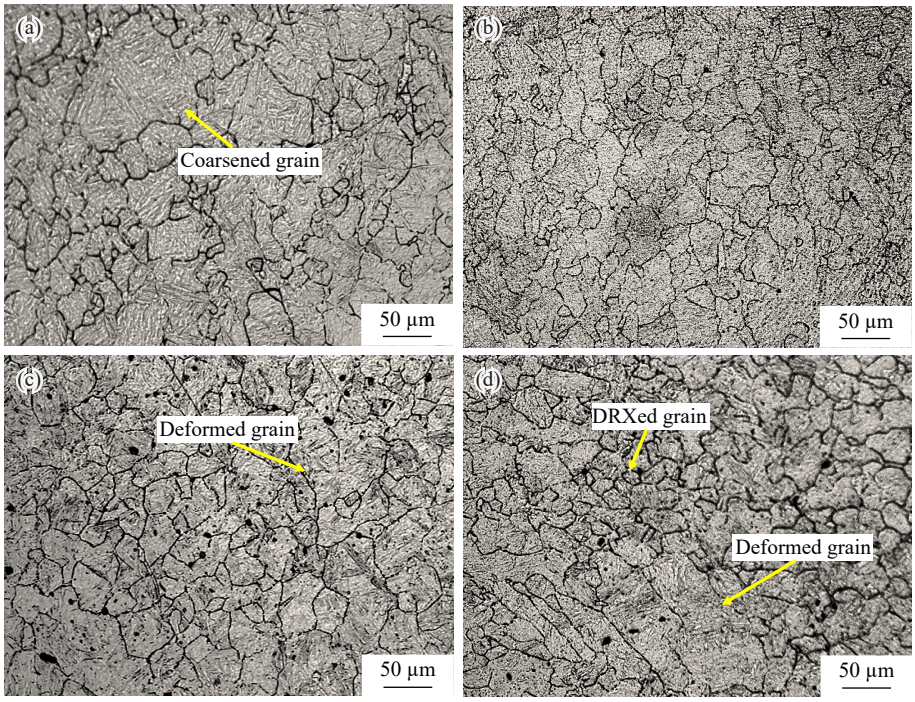

Fig. 10. Optical images of the microstructures in 5Mn (a, c) and 5MnNbV (b, d) after hot deformation (a, b) at 1100°C with strain rate of 0.1 s^{-1} and (c, d) at 1100°C with strain rate of 1 s^{-1}.

al examinations confirm the validity of the derived process maps in Fig. 9 and the significant improvement in the hot workability of MMS by Nb–V alloying.

4. Conclusions

Hot compression tests were performed on Nb–V microalloyed and free MMSs at temperatures of 1000–1150°C with strain rates of 0.001–1 s^{-1}. The flow curves of the two steels were simulated by the established constitutive equations, from which the deformation activation energy and processing maps were constructed to identify the unstable region. Combining the above with the microstructural examination results, the following conclusions are drawn.

(1) For the two studied MMS, most flow curves exhibit distinct peaks and a subsequent flattening, indicating the occurrence of DRX. Moreover, Nb–V microalloying strongly retards DRX during the hot deformation of MMS.

(2) Under the same hot deformation condition, Nb–V microalloying leads to high peak stress. The difference in critical strain between 5MnNbV and 5Mn steels decreases with the increase in deformation temperature, suggesting that NbC precipitates could retard DRX more efficiently than solute Nb in the studied temperature range.

(3) Nb–V microalloying also results in a significant increase in the deformation activation energy of 5Mn from ~378 to ~416 kJ/mol. Since the reported activation energy for some high Mn steels is in between these two values, we propose that Nb–V alloying could produce stronger retardation on DRX than high Mn content.

(4) Comparisons of hot deformation activation energy and processing maps show that Nb–V microalloying results in the reduced dependence of Q value on temperature and strain rate and a large region of stability. As a consequence, the hot workability of MMS is improved by narrowing the hot processing window for the unstable flow stress, in which fine recrystallized and coarse unrecrystallized grains are present.

Acknowledgements

Haiwen Luo gratefully acknowledges the continuous financial support from the National Natural Science Foundation of China (Nos. 52233018 and 51831002) and the China Baowu Low Carbon Metallurgy Innovation Foudation (No. BWLCF202213).

Conflict of Interest

Haiwen Luo is an editorial board member for this journal and was not involved in the editorial review or the decision to publish this article. The authors declare that they have no known competing financial interests or personal relationships that could have appeared to influence the work reported in this paper.

References

[1] A. Grajcar, R. Kuziak, and W. Zalecki, Third generation of AHSS with increased fraction of retained austenite for the automotive industry, *Arch. Civ. Mech. Eng.*, 12(2012), No. 3, p. 334.

[2] B. Hu, H. Sui, Q.H. Wen, Z. Wang, A. Gramlich, and H.W. Luo, Review on the plastic instability of medium-Mn steels for identifying the formation mechanisms of Lüders and Portevin–Le Chatelier bands, *Int. J. Miner. Metall. Mater.*, 31(2024), No. 6, p. 1285.

[3] B.B. He, B. Hu, H.W. Yen, *et al.*, High dislocation density-in-

duced large ductility in deformed and partitioned steels, *Science*, 357(2017), No. 6355, p. 1029.
[4] S.S. Li and H.W. Luo, Medium-Mn steels for hot forming application in the automotive industry, *Int. J. Miner. Metall. Mater.*, 28(2021), No. 5, p. 741.
[5] J.W. Zhao and Z.Y. Jiang, Thermomechanical processing of advanced high strength steels, *Prog. Mater. Sci.*, 94(2018), p. 174.
[6] Y.J. Wang, S. Zhao, R.B. Song, and B. Hu, Hot ductility behavior of a Fe–0.3C–9Mn–2Al medium Mn steel, *Int. J. Miner. Metall. Mater.*, 28(2021), No. 3, p. 422.
[7] G.Z. Quan, X. Wang, Y.L. Li, and L. Zhang, Analytical descriptions of dynamic softening mechanisms for Ti–13Nb–13Zr biomedical alloy in single phase and two phase regions, *Arch. Metall. Mater.*, 62(2017), No. 4, p. 2029.
[8] T. Sakai, A. Belyakov, R. Kaibyshev, H. Miura, and J.J. Jonas, Dynamic and post-dynamic recrystallization under hot, cold and severe plastic deformation conditions, *Prog. Mater. Sci.*, 60(2014), p. 130.
[9] J. Han, S.J. Lee, J.G. Jung, and Y.K. Lee, The effects of the initial martensite microstructure on the microstructure and tensile properties of intercritically annealed Fe–9Mn–0.05C steel, *Acta Mater.*, 78(2014), p. 369.
[10] H.B. Feng, S.H. Li, K.X. Wang, *et al*., Effect of deformation parameters on the austenite dynamic recrystallization behavior of a eutectoid pearlite rail steel, *Int. J. Miner. Metall. Mater.*, 31(2024), No. 5, p. 833.
[11] X.Y. Sun, M. Zhang, Y. Wang, Y.Y. Sun, and Y.H. Wang, Kinetics and numerical simulation of dynamic recrystallization behavior of medium Mn steel in hot working, *Steel Res. Int.*, 91(2020), No. 7, art. No. 1900675.
[12] X.Z. Liu, Y. Sun, X.Y. Zhang, H.P. Li, Z.C. Li, and L.F. He, Thermal deformation behavior and microstructure evolution of Fe−8.5Mn−1.5Al light-weight medium manganese steel, *J. Mater. Res. Technol.*, 26(2023), p. 605.
[13] T. Niu, Y.L. Kang, H.W. Gu, Y.Q. Yin, M.L. Qiao, and J.X. Jiang, Effect of Nb on the dynamic recrystallization behavior of high-grade pipeline steels, *Int. J. Miner. Metall. Mater.*, 17(2010), No. 6, p. 742.
[14] B.H. Chen and H. Yu, Hot ductility behavior of V–N and V–Nb microalloyed steels, *Int. J. Miner. Metall. Mater.*, 19(2012), No. 6, p. 525.
[15] Y. Luo, H.Z. Lu, N. Min, W. Li, and X.J. Jin, Effect of Mo and Nb on mechanical properties and hydrogen embrittlement of hot-rolled medium-Mn steels, *Mater. Sci. Eng. A*, 844(2022), art. No. 143108.
[16] R.S. Varanasi, B. Gault, and D. Ponge, Effect of Nb micro-alloying on austenite nucleation and growth in a medium manganese steel during intercritical annealing, *Acta Mater.*, 229(2022), art. No. 117786.
[17] Y.S. Zhu, B. Hu, and H.W. Luo, Influence of Nb and V on microstructure and mechanical properties of hot–rolled medium Mn steels, *Steel Res. Int.*, 89(2018), No. 9, art. No. 1700389.
[18] P.P. Singh, S. Ghosh, and S. Mula, Flow stress modeling and microstructural characteristics of a low carbon Nb–V microalloyed steel, *Mater. Today Commun.*, 30(2022), art. No. 103156.
[19] N. Tsuji, Y. Matsubara, and Y. Saito, Dynamic recrystallization of ferrite in interstitial free steel, *Scripta. Mater.*, 37(1997), No. 4, p. 477.
[20] X.H. Wang, Z.B. Liu, and H.W. Luo, Hot deformation characterization of ultrahigh strength stainless steel through processing maps generated using different instability criteria, *Mater. Charact.*, 131(2017), p. 480.
[21] K.M. Liu, Z.Y. Jiang, H.T. Zhou, D.P. Lu, A. Atrens, and Y.L. Yang, Effect of heat treatment on the microstructure and properties of deformation-processed Cu–7Cr *in situ* composites, *J. Mater. Eng. Perform.*, 24(2015), No. 11, p. 4340.
[22] D.L. Yin, K.F. Zhang, G.F. Wang, and W.B. Han, Warm deformation behavior of hot-rolled AZ31 Mg alloy, *Mater. Sci. Eng. A*, 392(2005), No. 1-2, p. 320.
[23] E.I. Poliak and J.J. Jonas, A one-parameter approach to determining the critical conditions for the initiation of dynamic recrystallization, *Acta Mater.*, 44(1996), No. 1, p. 127.
[24] G.J. Richardson, C.M. Sellars, and W.J.M. Tegart, Recrystallization during creep of nickel, *Acta Metall.*, 14(1966), No. 10, p. 1225.
[25] C.M. Sellars and W.J.McG. Tegart, Hot workability, *Int. Metall. Rev.*, 17(1972), No. 1, p. 1.
[26] H. Mirzadeh, J.M. Cabrera, J.M. Prado, and A. Najafizadeh, Hot deformation behavior of a medium carbon microalloyed steel, *Mater. Sci. Eng. A*, 528(2011), No. 10-11, p. 3876.
[27] Y.V.R.K. Prasad, H.L. Gegel, S.M. Doraivelu, *et al*., Modeling of dynamic material behavior in hot deformation: Forging of Ti-6242, *Metall. Trans. A*, 15(1984), No. 10, p. 1883.
[28] H. Mirzadeh, A. Najafizadeh, and M. Moazeny, Flow curve analysis of 17-4 PH stainless steel under hot compression test, *Metall. Mater. Trans. A*, 40(2009), No. 12, p. 2950.
[29] H.J. McQueen and N.D. Ryan, Constitutive analysis in hot working, *Mater. Sci. Eng. A*, 322(2002), No. 1-2, p. 43.
[30] H.J. McQueen and D.L. Bourell, Hot workability of metals and alloys, *JOM*, 39(1987), No. 9, p. 28.
[31] J.Q. Zhang, H.S. Di, X.Y. Wang, Y. Cao, J.C. Zhang, and T.J. Ma, Constitutive analysis of the hot deformation behavior of Fe–23Mn–2Al–0.2C twinning induced plasticity steel in consideration of strain, *Mater. Des.*, 44(2013), p. 354.
[32] D.J. Li, Y.R. Feng, Z.F. Yin, *et al*. Hot deformation behavior of an austenitic Fe–20Mn–3Si–3Al transformation induced plasticity steel, *Mater. Des.*, 34(2012), p. 713.
[33] H.J. McQueen, S. Yue, N.D. Ryan, and E. Fry, Hot working characteristics of steels in austenitic state, *J. Mater. Process. Technol.*, 53(1995), No. 1-2, p. 293.
[34] F. Reyes-Calderón, I. Mejía, and J.M. Cabrera, Hot deformation activation energy (Q_{HW}) of austenitic Fe–22Mn–1.5Al–1.5Si–0.4C TWIP steels microalloyed with Nb, V, and Ti, *Mater. Sci. Eng. A*, 562(2013), p. 46.
[35] A. Momeni, The physical interpretation of the activation energy for hot deformation of Ni and Ni–30Cu alloys, *J. Mater. Res.*, 31(2016), No. 8, p. 1077.
[36] D. Samantaray, S. Mandal, V. Kumar, S.K. Albert, A.K. Bhaduri, and T. Jayakumar, Optimization of processing parameters based on high temperature flow behavior and microstructural evolution of a nitrogen enhanced 316L(N) stainless steel, *Mater. Sci. Eng. A*, 552(2012), p. 236.
[37] S. Wang, L.G. Hou, J.R. Luo, J.S. Zhang, and L.Z. Zhuang, Characterization of hot workability in AA 7050 aluminum alloy using activation energy and 3-D processing map, *J. Mater. Process. Technol.*, 225(2015), p. 110.
[38] Y.V.R.K. Prasad and T. Seshacharyulu, Modelling of hot deformation for microstructural control, *Int. Mater. Rev.*, 43(1998), No. 6, p. 243.
[39] Y. Sun, W.D. Zeng, Y.Q. Zhao, X.M. Zhang, Y. Shu, and Y.G. Zhou, Research on the hot deformation behavior of Ti40 alloy using processing map, *Mater. Sci. Eng. A*, 528(2011), No. 3, p. 1205.